



# Co<sub>3</sub>O<sub>4</sub>-pillared montmorillonite catalysts synthesized by hydrogel-assisted route for total oxidation of toluene

Anna Rokicińska<sup>a</sup>, Piotr Natkański<sup>a</sup>, Barbara Dudek<sup>a</sup>, Marek Drozdek<sup>a</sup>, Lidia Lityńska-Dobrzańska<sup>b</sup>, Piotr Kuśtrowski<sup>a,\*</sup>

<sup>a</sup> Department of Chemical Technology, Faculty of Chemistry, Jagiellonian University, Ingardena 3, 30-060 Kraków, Poland

<sup>b</sup> Institute of Metallurgy and Materials Science, Polish Academy of Sciences, Reymonta 25, 30-059 Kraków, Poland



## ARTICLE INFO

### Article history:

Received 19 February 2016

Received in revised form 2 May 2016

Accepted 4 May 2016

Available online 6 May 2016

### Keywords:

Hydrogel-clay composites

Poly(acrylic acid)

Montmorillonite-based catalysts

Co<sub>3</sub>O<sub>4</sub>

Toluene combustion

## ABSTRACT

Montmorillonite (MT) pillared by Co<sub>3</sub>O<sub>4</sub> nanocrystallites was synthesized by the developed hydrogel-assisted route. In the first modification step, poly(acrylic acid) (PAA) was intercalated into the interlayer galleries of natural clay. Subsequently, Co<sup>2+</sup> ions were deposited in the structure of the formed composite by adsorption at controlled pH (3.3–9.0). The Co-modified samples were finally calcined at 500 °C in order to remove the hydrogel template. It was shown by FTIR and UV-vis-DR that Co<sup>2+</sup> cations interact with carboxyl groups distributed along the PAA chains and infiltrate effectively the clay interlayers. The random distribution of Co<sup>2+</sup> cations results in disordering of clay structure, confirmed by XRD and TEM. At the increasing pH of deposition more Co<sup>2+</sup> cations are bounded by the dissociated COO<sup>−</sup> groups. On the other hand, precipitation of Co hydroxide becomes a dominant way of transition metal deposition at the highest pH. The appearance of Co<sub>3</sub>O<sub>4</sub> nanoparticles between exfoliated montmorillonite platelets results in the expansion of pore system, and surface area and pore volume (generated mainly by the presence of mesopores) increase. Furthermore, temperature-programmed reduction (TPR) and X-ray photoelectron spectroscopy (XPS) revealed differences in reducibility and surface composition of the calcined materials. The developed materials appeared to be very active, selective and stable catalysts of toluene combustion. The best catalytic performance was found for the sample based on the precursor modified with Co<sup>2+</sup> at pH = 8.0, which exhibited 20%, 50% and 90% conversion of toluene at temperatures as low as 270 °C, 284 °C and 297 °C, respectively.

© 2016 Elsevier B.V. All rights reserved.

## 1. Introduction

Volatile organic compounds (VOCs) are high vapor pressure and low water solubility compounds, emitted to the atmosphere from many natural and anthropogenic sources. These compounds contribute to the formation of ground-level ozone, which is harmful to human health and vegetation [1]. Furthermore, VOCs have an abundant range of health effects on animals and humans, including cancer, throat irritation, respiratory issues or memory impairment [2,3]. Therefore, different physical, chemical and biological methods of VOCs elimination based on recovery (e.g. absorption, adsorption, condensation, membrane separation) or destruction (e.g. bio-filtration, thermal, catalytic and photocatalytic oxidation) have been developed [4,5]. The versatile and economical catalytic oxidation has been recognized as the most efficient method rec-

ommended for the removal of VOCs from the low concentration emission sources (<5000 ppm) [6,7]. Due to relatively low operating temperatures and using selective catalysts, the formation of detrimental byproducts (such as dioxins and NO<sub>x</sub>) during the catalytic oxidation of VOCs is also avoided. The highest catalytic activity in the VOCs combustion is observed over supported noble metals. Because these catalysts are relatively expensive and highly sensitive to deactivation by various impurities (e.g. S- and Cl-containing compounds), significantly cheaper and more stable transition metal oxide-based catalysts are often considered as a possible alternative [8,9].

Toluene, which has serious effects on the human central nervous system and is evolved from many sources such as crude petroleum and natural gas extraction, petroleum refining and household furniture manufacturing facilities, has been often chosen as a representative of aromatic VOCs for searching of optimal technique of their elimination. Thus, the total oxidation of toluene has been tested over a wide variety of different mono-, bi- or multicomponent catalysts containing noble metals (e.g. Au [10–15],

\* Corresponding author.

E-mail address: [kustrows@chemia.uj.edu.pl](mailto:kustrows@chemia.uj.edu.pl) (P. Kuśtrowski).

Ag [10], Pt [13,16,17], Pd [12–16,18,19]), transition metals (e.g. Mn [20–30], Cu [10,21,22,27,29,31–34], Co [18,21,24,32,33,35–37], Fe [21,38,35,39]) or lanthanides (e.g. Ce [14,22,27,34,40]). The active phase was often deposited on different supports (such as  $\text{Al}_2\text{O}_3$  [17,20,22,28,34],  $\text{TiO}_2$  [12–14,16],  $\text{CeO}_2$  [10,14,17],  $\text{ZrO}_2$  [27], mesoporous silicas [15,35,37,39]), or incorporated into the structure of perovskites [30,36,38], hydrotalcite-derived mixed oxides [18,21,24], clays [33,40], and zeolites [19,41,42].  $\text{Co}_3\text{O}_4$ -containing materials have been shown to be one of the most efficient non-noble metal oxides for the VOCs elimination.  $\text{Co}_3\text{O}_4$  is a normal spinel with a cubic close-packing array of oxide ions, in which  $\text{Co}^{2+}$  ions occupy the tetrahedral 8a sites, and  $\text{Co}^{3+}$  – the octahedral 16d sites [43]. The relatively high concentration of electrophilic O<sup>–</sup> species on highly strained  $\text{Co}_3\text{O}_4$  nanocrystals with an enhanced lattice distortion results in an easy interaction between the oxygen lattice atoms and the organic molecules and a high catalytic activity in the VOCs combustion [44]. Additional parameters favoring the superior activity of  $\text{Co}_3\text{O}_4$  are its improved reducibility and high concentration of oxygen vacancies [45,46]. Recently, Gomez et al. [47] proved that the total oxidation of toluene proceeds according to the Mars–van Krevelen mechanism over  $\text{Co}_3\text{O}_4$ -based catalysts. They postulated that during the initial reaction step,  $\text{O}_2$  is adsorbed at the surface vacancies forming highly active species, which activate toluene molecules by dehydrogenation of methyl groups. The activated toluene is subsequently oxidized by lattice oxygen. Finally, gas phase  $\text{O}_2$  re-oxidizes the reduced catalyst.

Natural clays provide an ideal platform to support the catalytically active phase. Many different approaches are known, which allow to generate active sites and open the porous structure of these materials. The pillared clays (PILCs) with highly expanded porosity can be excellent examples of supports for dispersion of noble metals and transition metal oxides exhibiting good catalytic performance in the VOCs combustion [48]. Nevertheless, it should be kept in mind that the expensive and time-consuming production of PILCs is based on the incorporation of pillars formed by stable metal oligocations (e.g. Ti, Zr, Al, Fe), and the obtained PILCs still have to be modified with the precursor of noble- or transition metal-containing active phase. In our recent paper [49], we demonstrated a very effective method of clay modification, which can be applied to obtain materials containing transition metal oxides dispersed on an exfoliated mineral. Firstly, polymer hydrogel is intercalated into a clay structure to form a clay–polymer composite with an enhanced metal cation adsorption capacity. The synthesized composite is subsequently modified with transition metal cations by controlled deposition. Finally, the composite is calcined and the stable material with a highly dispersed active phase and an expanded surface area is formed. In the presented work, we have adopted this synthesis procedure to fabricate  $\text{Co}_3\text{O}_4$ -pillared montmorillonite, which appeared to be excellent catalysts for the toluene combustion. The influence of pH used during the  $\text{Co}^{2+}$  ions deposition in the clay/hydrogel composite on dispersion and catalytic performance of  $\text{Co}_3\text{O}_4$  has been studied.

## 2. Experimental

### 2.1. Synthesis

The clay mineral (MT) used in this work was Slovak bentonite Jelšový potok (processed by ZGM Zębiec S.A. in Poland and available as a commercial product Bentonit Specjal) with the content of montmorillonite higher than 75 wt%. Its cation exchange capacity (CEC) was 86 meq/100 g. The chemical composition of the studied MT, determined by X-ray fluorescence spectroscopy (XRF), is shown in Table 1.

**Table 1**

Chemical composition (in mass ratios) of MT and  $\text{Co}^{2+}$ -adsorbed MT-PAA composites after calcination at 500 °C.

Catalyst	Al/Si	Mg/Si	Fe/Si	Ca/Si	K/Si	Na/Si	Co/Si	bulk <sup>a</sup>	surface <sup>b</sup>
							–		
MT	0.30	0.07	0.05	0.05	0.02	0.06	–	–	–
MT-PAA pH 3.3 calc	0.31	0.07	0.06	0.01	0.02	–	0.18	0.35	
MT-PAA pH 4.0 calc	0.31	0.07	0.06	0.01	0.02	–	0.31	0.42	
MT-PAA pH 5.0 calc	0.32	0.07	0.05	0.03	0.02	0.02	0.77	0.56	
MT-PAA pH 6.0 calc	0.32	0.07	0.05	0.04	0.02	0.04	0.85	0.72	
MT-PAA pH 7.0 calc	0.33	0.07	0.05	0.04	0.02	0.12	0.87	0.66	
MT-PAA pH 8.0 calc	0.32	0.06	0.05	0.04	0.02	0.17	0.93	0.70	
MT-PAA pH 9.0 calc	0.33	0.04	0.06	0.04	0.02	0.63	1.03	1.02	

<sup>a</sup> determined by XRF.

<sup>b</sup> determined by XPS.

The clay/hydrogel composite was prepared by the in situ intercalative polymerization technique. Acrylic acid (AA, Arkema) and N,N'-methylenebisacrylamide (NMBA, Sigma-Aldrich) were dissolved in distilled water at the NMBA/AA molar ratio of 0.01 to obtain 1000 mL of 6 wt% solution. Subsequently, the clay was introduced at the MT/AA mass ratio of 1:1. The mixture was agitated with a mechanical stirrer (300 rpm) at room temperature to produce a homogenous suspension. Then, oxygen was removed by purging of argon for 30 min, and ammonium persulfate (APS, Sigma-Aldrich) was added at the APS/AA molar ratio of 0.01. The mixture was heated to 65 °C and kept at this temperature for 3 h to ensure the complete polymerization of monomers. The synthesized composite (MT-PAA) was shredded in a cutting mill, dried at 60 °C and grinded to fine powder (<125  $\mu\text{m}$ ). The PAA content in the formed MT-PAA composite, determined by thermogravimetric analysis (TG), was 40.3 wt%.

In the subsequent step, the MT-PAA composite was modified by adsorption of  $\text{Co}^{2+}$  cations at controlled pH (ranging from 3.3 to 9.0). At each case, 2 g of dried MT-PAA was introduced into an aqueous solution of  $\text{Co}(\text{NO}_3)_2$  (500 mL, 0.01 M) at 30 °C and pH was adjusted by an addition of suitable amount of 0.1 M NaOH solution. During the  $\text{Co}^{2+}$  deposition, the slurry was stirred with a magnetic stirrer (400 rpm). After 24 h, the material was isolated by filtration, washed with deionized water several times and dried at 65 °C. Finally, the hydrogel template was removed from the samples by calcination in a tube furnace in flowing air (33 mL/min) at 500 °C for 6 h with a heating rate of 1 °C/min. The Co-containing samples were designated as MT-PAA pH x, where x represents the pH value used during the deposition.

### 2.2. Characterization

Chemical analysis of all samples was performed by XRF using a Thermo Scientific ARL Quant'x spectrometer. Powder X-ray diffraction (XRD) patterns were recorded using a Bruker D2 Phaser diffractometer with  $\text{CuK}\alpha$  radiation ( $\lambda = 1.54056 \text{ \AA}$ ). Prior to these measurements the studied samples were dried at 60 °C for 24 h. The diffractograms were collected in the 2 $\theta$  range of 0.5–50° with a scanning rate of 0.02°. All samples were examined in a powder form. Infrared spectra were recorded by means of a Nicolet 6700 FT-IR spectrometer equipped with a MCT-A detector and DRIFT accessory in the wavenumber range of 650–4000  $\text{cm}^{-1}$  at 4  $\text{cm}^{-1}$  resolution. The dried materials were ground with potassium bromide to obtain mixtures containing 10 wt% of the measured sample. UV–vis diffuse reflectance spectra were collected using a Thermo Scientific Evolution 220 spectrometer in the range of 200–900 nm with resolution of 1 nm collecting 60 scans per minute. Thermal stability of the as-synthesized samples was examined in a TA Instruments SD Q600 thermoanalyzer. Thermogravimetry (TG) and differential thermal analysis (DTA) were carried out using about

10 mg of a sample in an air atmosphere (a flow rate of 100 mL/min) from 30 to 1000 °C at a heating rate of 20 °C/min. Textural properties of the calcined samples were determined by low-temperature adsorption of nitrogen using a Micromeritics ASAP 2020 sorptometer. Before the measurements, samples were outgassed at 250 °C for 5 h under vacuum. Transmission electron microscopy (TEM) images were taken using a Tecnai G2 F20 transmission electron microscope equipped with a field emission gun operating at 200 kV. Samples in a powder form were placed on a copper grid and then coated by carbon.

X-ray photoelectron spectrometer (XPS) spectra analyses were conducted using a Prevac photoelectron spectrometer equipped with a monochromatized aluminium source AlK $\alpha$  ( $E = 1486.6$  eV) and a hemispherical VG SCIENTA R3000 analyzer. Samples were introduced through a load lock into an ultrahigh vacuum analytical chamber with the base pressure of  $5 \times 10^{-9}$  mbar. To compensate the charge on the surface of nonconductive samples, a low energy electron flood gun (FS40A-PS) was used. The scale of the binding energy value was adjusted by reference of the Si 2p peak at 103.0 eV. The spectra were fitted with Casa XPS software.

Temperature-programmed reduction (TPR) measurements were conducted using a SDT Q600 thermogravimeter (TA Instruments). An amount of 10 mg of a sample was placed in a corundum crucible in the flow of argon containing 10 vol.% of H<sub>2</sub> (60 mL/min) and heated from 30 °C to 1000 °C at a heating rate of 20 °C/min. The TPR profiles were determined on the base of mass losses related to the removal of lattice oxygen during the reduction process.

### 2.3. Catalytic activity

The synthesized materials were tested as catalysts in the total oxidation of toluene. 0.1 g of a catalyst, comminuted and sieved to a particle size of 160–315  $\mu$ m, was placed in a central position of quartz flow microreactor on a quartz wool plug and outgassed, prior to a catalytic run, at 500 °C for 30 min in flowing air (100 mL/min). Then, the reactor was cooled down to 200 °C and toluene dosing started by passing air through a saturator (kept at –17.5 °C) to achieve the toluene vapor concentration of 1000 ppm in the reaction mixture. The catalytic tests were carried out at 200, 250, 275, 300, 325, 350, 400, 450 and 500 °C. The reactor was kept at each temperature (reached at a heating rate of 10 °C/min) for 80 min with three 25-min lasting analyses of reaction products conducted using a Bruker 450-GC gas chromatograph equipped with three columns (Molecular Sieve 5A for separation of O<sub>2</sub>, N<sub>2</sub> and CO, Porapak S for separation of CH<sub>4</sub>, CO<sub>2</sub> and H<sub>2</sub>O, and Chromosorb WAW-DMCS for separation of aromatic compounds), a thermal conductivity detector, two flame ionization detectors as well as a methaniser.

## 3. Results and discussion

### 3.1. Characterization of MT-PAA composites after deposition of Co<sup>2+</sup> cations

The XRD patterns of MT (dried at 60 °C), MT-PAA and the samples after deposition of Co<sup>2+</sup> cations (MT-PAA pH x) are presented in Fig. 1. In the case of the raw material, the diffraction lines characteristic of layered structure of montmorillonite observed at 9.1°, 18.5°, 19.9° and 28.0° correspond to the (001), (002), (-111) and (003) reflections [PDF 00-060-0321]. The (001) peaks, attributed to the formation of the interlayer spaces by regular stacking of the silicate layers, reveal the basal spacing of 0.96 nm. Moreover, the recorded XRD pattern exhibits the presence of crystalline impurities in the studied MT. Among them, the admixture of quartz, manifested by the peaks at 20.9°, 26.7° and 36.6° [PDF 00-001-

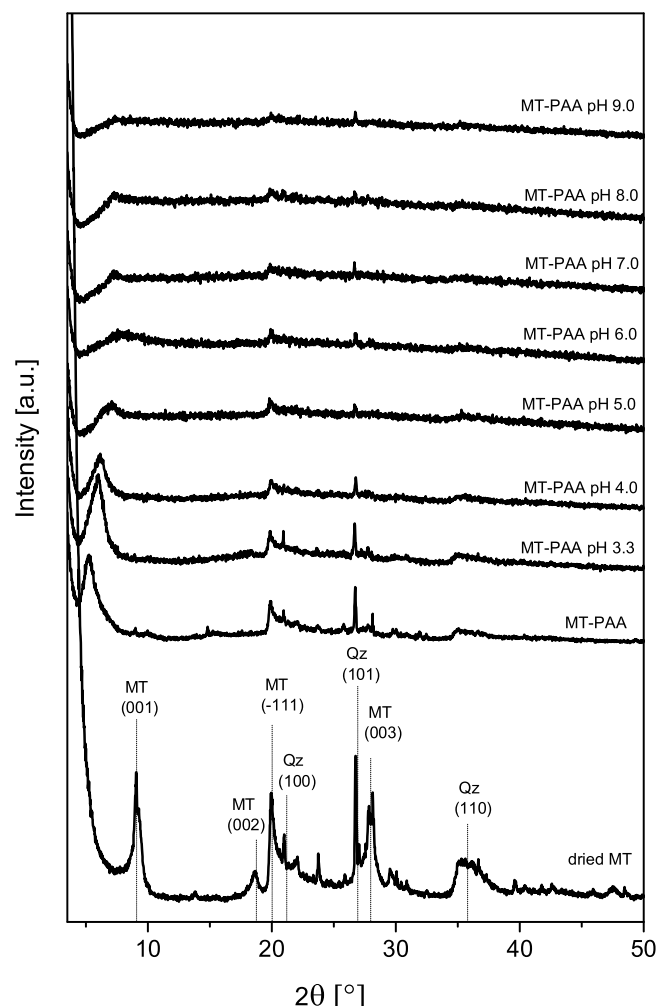
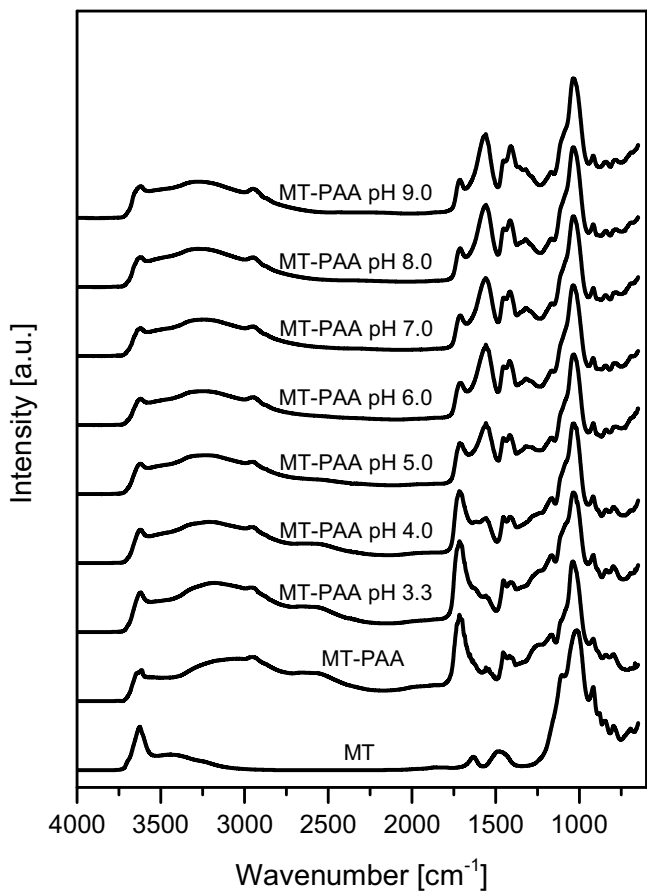


Fig. 1. XRD patterns of dried MT as well as MT-PAA composite before and after deposition of Co<sup>2+</sup> cations.

0649], is the most distinct. The interlayer distance of MT increases to 1.67 nm after the introduction of hydrogel. It is clear that during the contact between monomers and clay, a part of organic molecules migrates to the interlayer space of MT and subsequently polymerizes there. The appearance of hydrogel in the interlayer galleries leads to their expansion. The formation of poly(acrylic acid)-intercalated MT structure was previously described by Tran et al. [50,51] and Natkański et al. [52], who found the increase in the interlayer space of PAA-modified MT to 1.58–1.88 nm. Nevertheless, it should be expected that the formed PAA is also deposited on the outer surface of MT [52]. The deposition of Co<sup>2+</sup> cations results in the decrease in the intensities of diffraction lines attributed to MT, which is especially deep in the case of (001) peak. These effects can be explained by dilution of the MT-PAA composite by Co species, the fluorescence effect arising from the copper radiation as well as random disordering of layered structure related to partial delamination, which is most likely associated with the infiltration of the interlayers by raising amounts of Co<sup>2+</sup> cations, as confirmed by XRF (Table 1).

The interaction between the MT-PAA composite and the introduced Co<sup>2+</sup> cations was studied by DRIFT. In Fig. 2 the IR spectra collected for the MT, MT-PAA and MT-PAA pH x materials are shown. In the presented DRIFT spectra, the bands characteristic of MT are observed mainly in two wavenumber ranges of 3000–3750 cm<sup>–1</sup> (stretching vibrations of OH groups) and 650–1250 cm<sup>–1</sup> [53,54]. Additionally, the bending vibrations of OH



**Fig. 2.** DRIFT spectra of dried MT as well as MT-PAA composite before and after deposition of  $\text{Co}^{2+}$  cations.

groups of water molecules adsorbed on MT are manifested by the band at  $1633\text{ cm}^{-1}$ . In the lower frequencies range, the main bands corresponding to the Si-O out-of-plane stretching vibrations ( $1105\text{ cm}^{-1}$ ), the Si-O in-plane stretching vibrations ( $1015\text{ cm}^{-1}$ ), as well as the bending vibrations of OH in Al-Al-OH (at  $920\text{ cm}^{-1}$ ) and in Al-Mg-OH (at  $845\text{ cm}^{-1}$ ) can be distinguished. Moreover, in the DRIFT spectrum of unmodified MT the characteristic bands attributed to the vibrations of carbonate anions mainly in the range of  $1400\text{--}1500\text{ cm}^{-1}$  are recognized.

Beside the vibrations typical of the MT structure, some additional bands related to the presence of PAA can be identified for the MT-PAA composite before and after deposition of  $\text{Co}^{2+}$  cations. The C-C and C-H modes, assigned to the backbone chains, are found at  $1460\text{ cm}^{-1}$  ( $\text{CH}_2$  deformation) and  $2950\text{ cm}^{-1}$  ( $\text{CH}_2$  stretching) [55]. Furthermore, the stretching vibrations of  $\text{C}=\text{O}$  groups are manifested by the presence of IR band at  $1717\text{ cm}^{-1}$  (for MT-PAA). The intensity of this band decreases gradually and its position shifts slightly to lower frequencies (finally to  $1708\text{ cm}^{-1}$  for MT-PAA pH 9.0) after the modification with  $\text{Co}^{2+}$  at the increasing pH. Simultaneously, the intensities of bands corresponding to the dissociated  $\text{COO}^-$  groups – at about  $1410\text{ cm}^{-1}$  (symmetric  $\text{COO}^-$  stretching) and  $1560\text{ cm}^{-1}$  (asymmetric  $\text{COO}^-$  stretching) [56] – increase. It means that  $\text{Co}^{2+}$  cations introduced into the MT-PAA composite structure are mainly bound by the strong ionic bonds between the metallic ions and the  $\text{COO}^-$  groups in the PAA chains. At the increasing pH the number of protons in the  $\text{Co}^{2+}$  nitrate solution used during adsorption continues to fall, and they lose competition with  $\text{Co}^{2+}$  ions for the adsorption sites. That is most likely a reason why we observe the increasing loading of Co with the raising pH. On the other hand, higher loadings of Na are found (cf. Table 1) due to

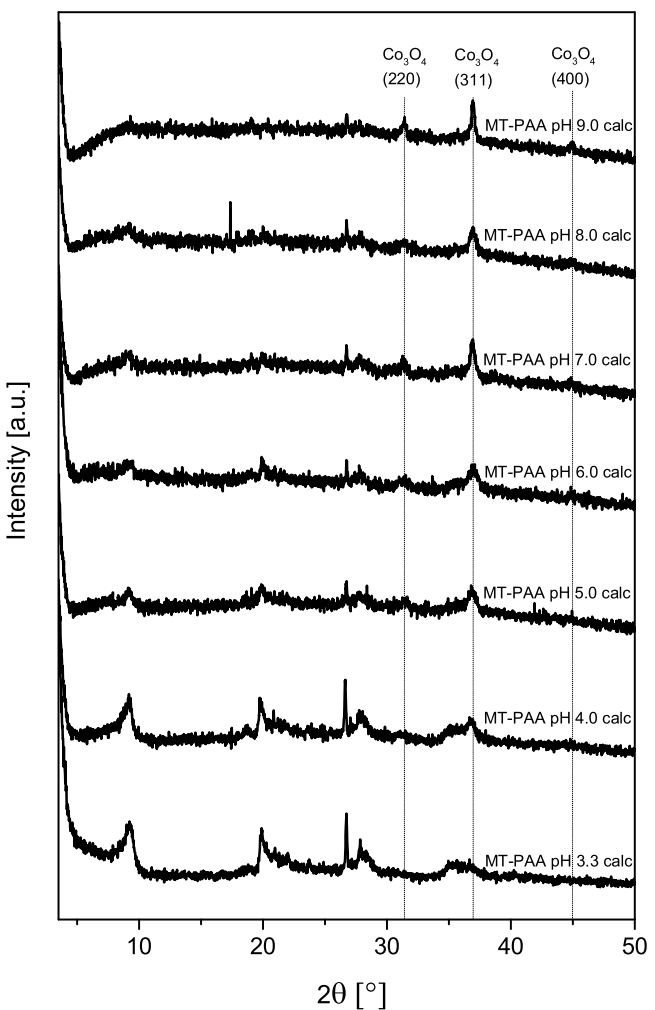


**Fig. 3.** XRD patterns of calcined Co-containing MT-PAA materials.

using of NaOH as a pH controlling agent. Its content is especially distinct after the modification of MT-PAA at pH = 9.0.

UV-vis-DR spectroscopy provides some additional information on the chemical environment of deposited cobalt cations. The spectra of dried MT-PAA and some chosen MT-PAA samples after modification with  $\text{Co}^{2+}$  are presented in Fig. S1. In the case of MT-PAA pH 3.3 the appearance of absorption band at about  $520\text{ nm}$ , which is related to the formation complexes between  $\text{Co}^{2+}$  ions and  $\text{COO}^-$  groups [57], confirms the successful introduction of transition metal cations into the composite structure. The increasing intensity of this band and its shift to higher wavelength values reveal the incorporation of higher Co amount at the raising pH (as found by XRF). On the other hand, the position of absorption bands in the region of  $480\text{--}580\text{ nm}$  [58] and the pink color of the modified materials confirm that the introduced cobalt ions are in the divalent state with the octahedral coordination. Nevertheless, at the highest pH a partial oxidation of  $\text{Co}^{2+}$  to  $\text{Co}^{3+}$  occurs, and the additional absorption band in the region of  $350\text{--}400\text{ nm}$ , assigned to  ${}^1\text{A}_{1g} \rightarrow {}^1\text{T}_{2g}$  transition in octahedral  $\text{Co}^{3+}$ , is observed [59]. Similar features exhibit the sample precipitated in the absence of MT-PAA at the same conditions (cf. Fig. S1). It should be noticed that intensification of  $\text{Co}(\text{OH})_2$  precipitation is observed at pH = 9.0 and therefore this pH seems to be too high to selective deposition of  $\text{Co}^{2+}$  in the clay/hydrogel composite structure.

To transform the synthesized Co-containing clay/hydrogel precursors into the thermally stable oxide-based catalysts, the PAA template was removed by calcination. The conditions of the ther-

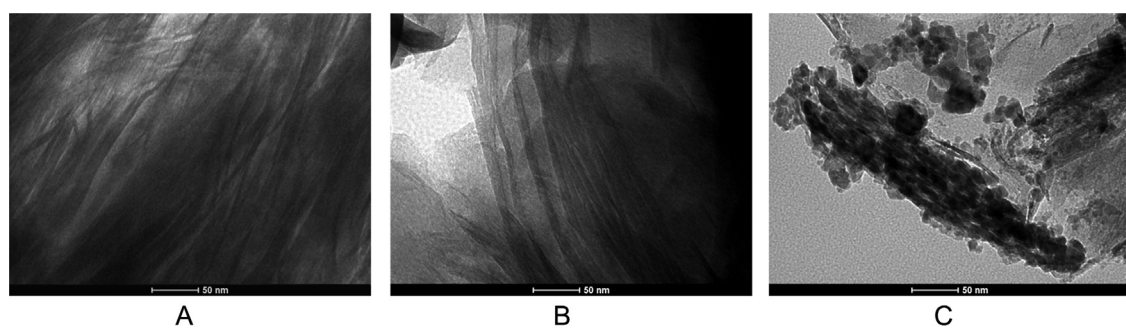


Fig. 4. TEM images of MT-PAA (A) and calcined MT-PAA after modification at pH = 6.0 before (B) and after (C) calcination at 500 °C.

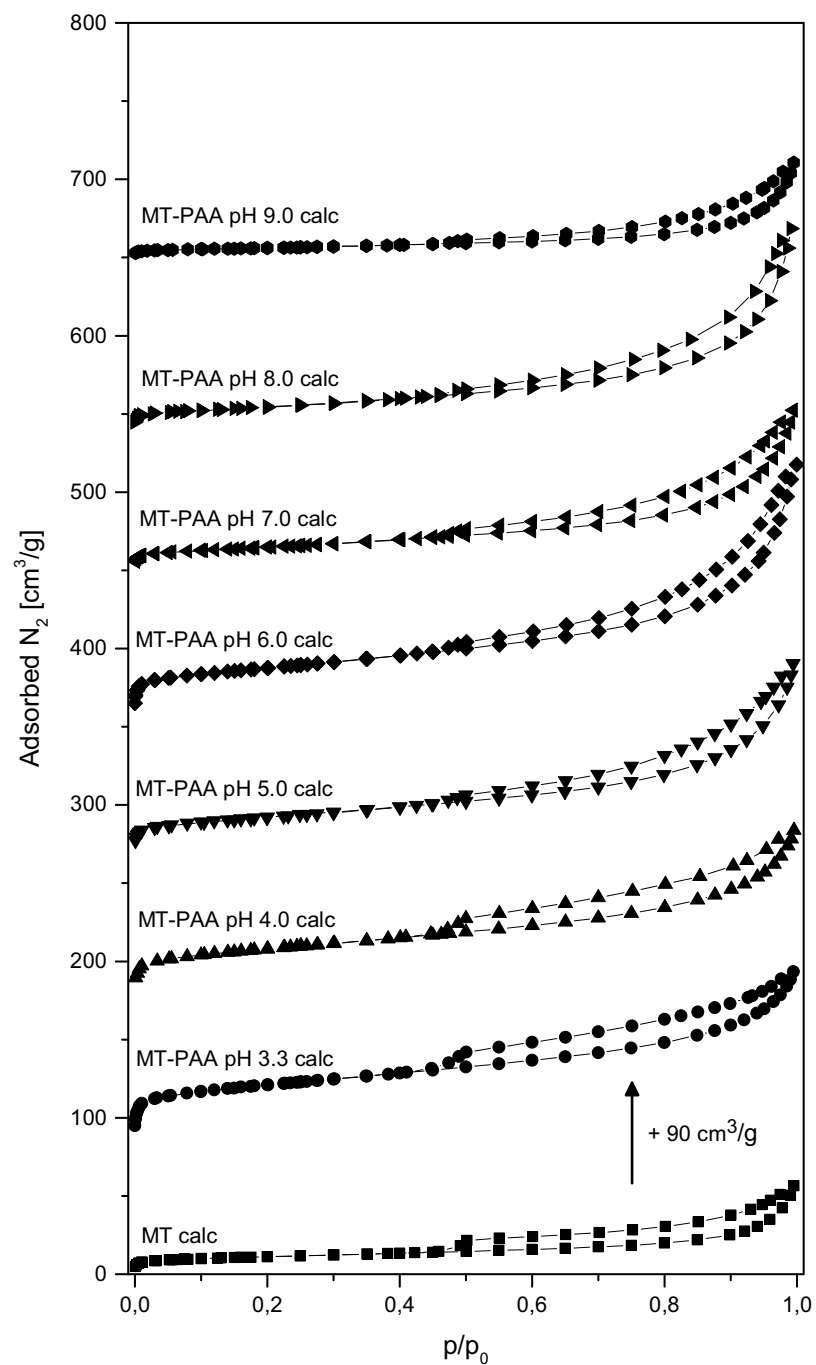
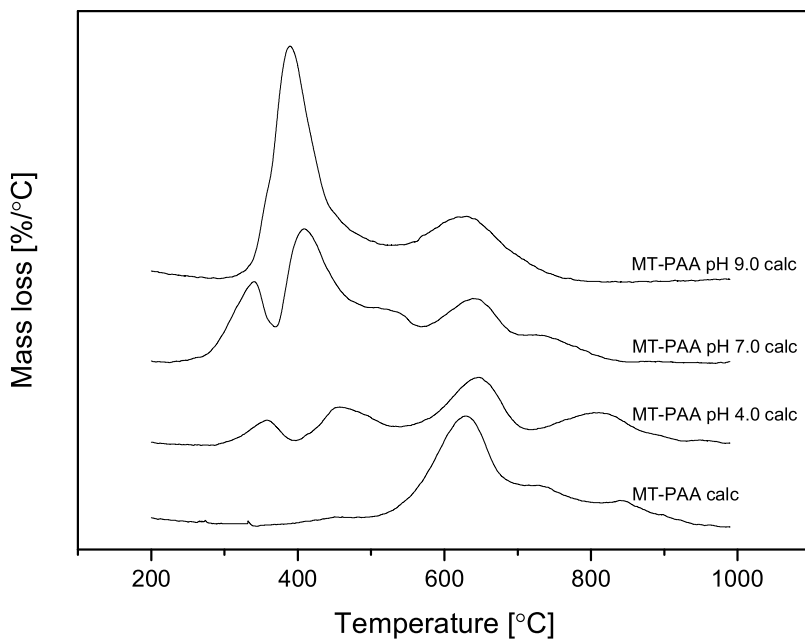


Fig. 5. Low-temperature  $\text{N}_2$  adsorption isotherms for calcined Co-containing MT-PAA materials.



**Fig. 6.** DTG profiles measured at reducing atmosphere for some selected calcined samples.

**Table 2**

Textural parameters, redox properties and catalytic activity of MT, MT-PAA and  $\text{Co}^{2+}$ -adsorbed MT-PAA composites after calcination at 500 °C.

Catalyst	Textural parameters				Reducibility			Conversion temperature [°C]		
	$S_{\text{BET}}$ [ $\text{m}^2/\text{g}$ ]	$V_{\text{meso}}$ [ $\text{cm}^3/\text{g}$ ]	$V_{\text{micro}}$ [ $\text{cm}^3/\text{g}$ ]	$V_{\text{total}}$ [ $\text{cm}^3/\text{g}$ ]	$T_{\text{max},1}$ [°C]	$T_{\text{max},2}$ [°C]	$\text{H}_2\text{,consum.}/\text{H}_2\text{,theor.}$	$T_{20}$ (20%)	$T_{50}$ (50%)	$T_{90}$ (90%)
MT	38	0.047	0.006	0.087	–	–	–	n.m.	n.m.	n.m.
MT-PAA calc	57	0.075	0.005	0.109	–	–	–	n.m.	n.m.	n.m.
MT-PAA pH 3.3 calc	108	0.119	0.007	0.160	384	476	0.49	340	365	394
MT-PAA pH 4.0 calc	98	0.119	0.005	0.161	357	457	0.61	305	313	325
MT-PAA pH 5.0 calc	79	0.144	0.003	0.186	339	451	0.89	277	286	297
MT-PAA pH 6.0 calc	98	0.173	0.003	0.244	334	443	0.96	276	285	297
MT-PAA pH 7.0 calc	53	0.111	0.001	0.158	339	410	0.94	278	288	301
MT-PAA pH 8.0 calc	53	0.129	0.001	0.199	335	415	0.93	270	284	297
MT-PAA pH 9.0 calc	22	0.056	0.001	0.094	390	–	0.92	307	342	426

mal treatment were chosen on the basis of thermogravimetric measurements (Fig. S2). Three crucial decomposition steps are distinguished in the TG and DTA curves measured for MT-PAA before and after  $\text{Co}^{2+}$  deposition. At low temperatures (up to 200 °C) physically adsorbed and interlayer water is eliminated. In turn, dehydroxylation of MT layers occurs above 550 °C, which is also observed for the unmodified clay. In the case of MT-PAA burning of polymer template is observed in the temperature range of 180–510 °C. For the Co-doped samples this decomposition effect is clearly shifted to lower temperatures with exception of MT-PAA pH 9.0, which shows a shoulder in the range of 450–500 °C, probably due to the presence of the precipitated Co species. The similar acceleration of hydrogel burning was previously found for the Fe-containing MT-PAA composites [49]. However, iron species were significantly more efficient in the oxidation of PAA compared to cobalt ones. Taking into account the observed effects the temperature of 500 °C was selected to the final transformation of the Co-modified MT-PAA composites into the thermally stable oxide materials.

### 3.2. Characterization of calcined $\text{Co}_3\text{O}_4$ -containing catalysts

The changes in the structure of the Co-containing MT-PAA samples after the thermal treatment were examined by XRD (Fig. 3). The performed calcination results in a clear shift of the (001) diffraction line towards higher  $2\theta$  values, which is observed at  $d = 0.96\text{--}0.98 \text{ nm}$

regardless to the Co content. The basal spacing of the studied materials comparable to that determined for the dried MT confirms the existence of part of ordered layered structure unmodified with Co species. On the other hand, the decreasing intensity of this reflection is observed at the raising Co loading due to (i) the appearance of Co oxide that causes the sample dilution and strong fluorescence arising from the copper radiation, as well as (ii) the partial exfoliation of the modified MT structure. The latter effect can be related to the formation of  $\text{Co}_3\text{O}_4$  nanocrystallites randomly between the sheets in the interlayer galleries containing the intercalated hydrogel template. The presence of  $\text{Co}_3\text{O}_4$  nanoparticle is confirmed by three diffraction lines observed at 31.4°, 36.9° and 44.9°  $2\theta$  corresponding to (220), (311) and (400) planes, respectively [PDF 00-009-0418]. The intensities of these peaks grow with the increase in the Co loading. It should however be noticed that the  $\text{Co}_3\text{O}_4$  crystallite size of 15–17 nm, estimated using the Scherrer equation (based on the (311) peak broadening), is similar for all studied materials with exception of MT-PAA pH 9.0 exhibiting significantly higher  $\text{Co}_3\text{O}_4$  crystallite size of about 27 nm. This distinctness of the sample obtained by deposition of  $\text{Co}^{2+}$  at the highest pH should be explained by the precipitation of Co hydroxide favoring the formation of larger oxide phase crystallites.

The postulated changes in the structure of the MT-PAA composite by adsorption of  $\text{Co}^{2+}$  cations and subsequent calcination at 500 °C were additionally confirmed by TEM. The images taken for MT-PAA before and after Co<sup>2+</sup> deposition at pH = 6.0 are shown

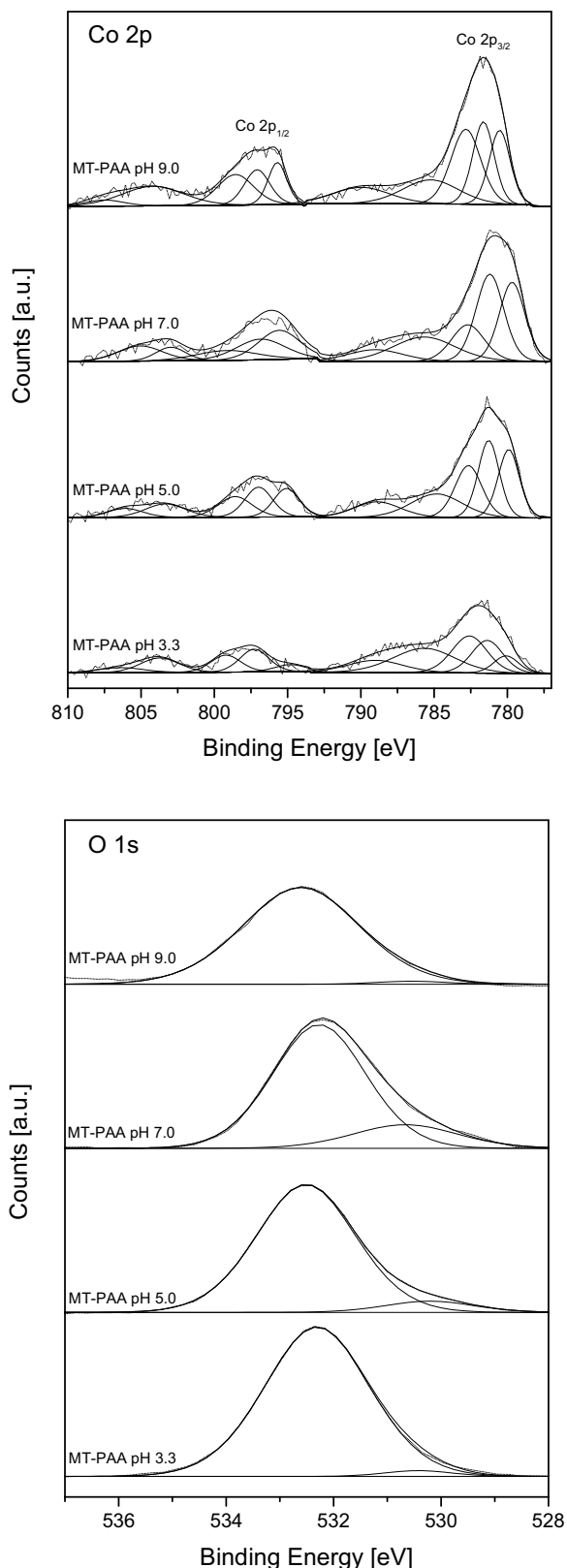


Fig. 7. Co 2p and O 1s XPS spectra of some selected calcined Co-containing samples.

in Fig. 4. It is clear that PAA is partially intercalated between the MT layers during the polymerization process (Fig. 4A). Furthermore, adsorption of  $\text{Co}^{2+}$  leads to a significant expansion of partially delaminated platelets due to breaking of hydrogen bonds engaging adjacent COOH groups of polymer and OH groups from the MT structure as well as infiltration of transition metal cations into the polymer located in the interlayers (Fig. 4B). After calcination, which results in burning of PAA, the composite structure collapses and the nanocrystallites of  $\text{Co}_3\text{O}_4$  (with size within the range of 2–30 nm) appear among the highly disordered montmorillonite platelets (Fig. 4C). It should be assumed that the highly dispersed spinel particles are well exposed to be active sites in catalytic processes, and, on the other hand, the clay structure protects them against sintering and aggregation.

Porosity of the calcined materials was studied by low-temperature nitrogen adsorption. The recorded isotherms are collected in Fig. 5, whereas the calculated textural parameters – pore size distribution (determined using the BJH model), specific surface area ( $S_{\text{BET}}$ , BET model), volume of micro- ( $V_{\text{micro}}$ , t-plot model) and mesopores ( $V_{\text{meso}}$ , BJH model) as well as total pore volume ( $V_{\text{total}}$ , single point method) – are presented in Fig. S3 and Table 2. As expected, the introduction of PAA into the MT structure and the subsequent deposition of  $\text{Co}_3\text{O}_4$  nanoparticles results in significant variations in the porosity of the calcined samples. The type II isotherm (according to the Brunauer, Deming, Deming and Teller (BDDT) classification) collected for MT, representing unrestricted multilayer adsorption on a surface of poorly porous solid, changes to the type IV isotherms in the case of the modified materials, which exhibit a capillary condensation step at high relative pressures typical of mesoporous solids. It should therefore be concluded that modification of MT opens its pore structure due to high dispersion of clay platelets. This effect is additionally enhanced by the formation of cobalt spinel nanoparticles, which pillar the MT sheets. The changes in the porosity of the samples are reflected in their textural parameters. An increase in the BET surface area and the mesopore volume is observed for the calcined MT-PAA ( $S_{\text{BET}} = 57 \text{ m}^2/\text{g}$ ,  $V_{\text{meso}} = 0.075 \text{ cm}^3/\text{g}$ ) and MT-PAA pH 3.3 ( $S_{\text{BET}} = 108 \text{ m}^2/\text{g}$ ,  $V_{\text{meso}} = 0.119 \text{ cm}^3/\text{g}$ ) samples in relation to the raw material ( $S_{\text{BET}} = 38 \text{ m}^2/\text{g}$ ,  $V_{\text{meso}} = 0.047 \text{ cm}^3/\text{g}$ ). The further raising Co content results in a gradual decrease in the BET surface area to  $22 \text{ m}^2/\text{g}$  (for MT-PAA pH 9.0) mainly due to the raising participation of non-porous  $\text{Co}_3\text{O}_4$  in the sample mass. On the other hand, the increasing amount of Co favors the formation of mesoporosity, which reaches the highest extent for the calcined MT-PAA pH 6.0 material ( $V_{\text{meso}} = 0.173 \text{ cm}^3/\text{g}$ ) and is confirmed by pore size distribution (Fig. S3). For the samples with the higher Co loadings, the lowering mesopore volume is observed. These findings are the most distinct for the MT-PAA pH 9.0 sample, which shows huge amounts of  $\text{Co}_3\text{O}_4$  nanocrystallites formed by decomposition of Co-containing precursor deposited by precipitation on the external surface of MT-PAA.

Examples of DTG profiles recorded for the calcined MT-PAA, MT-PAA pH 4.0, MT-PAA pH 7.0 and MT-PAA pH 9.0 catalysts in the flowing  $\text{H}_2 + \text{Ar}$  mixture in the temperature range of 200–1000 °C are shown in Fig. 6. Moreover, the temperatures of reduction maxima as well as the  $\text{H}_{2,\text{consumed}}/\text{H}_{2,\text{theor}}$  ratio between the real amount of consumed  $\text{H}_2$  and the theoretical one, calculated assuming the reduction of  $\text{Co}_3\text{O}_4$  to metallic Co, observed below the temperature of MT dehydroxylation are given in Table 2 for all samples. For the Co-free sample, the mass loss typical of the MT dehydroxylation, which intensifies at the temperatures above 550 °C, is observed. This peak remains in the DTG profiles of the Co-containing samples, however its intensity decreases due to the appearance of  $\text{Co}_3\text{O}_4$  phase lowering the relative MT content. For these catalysts some additional mass loss effects, related to the reduction of spinel phase, can be also identified. In the case of MT-PAA pH 3.3, two reduc-

tion peaks centered at 384 °C and 476 °C, which can be assigned to the successive reduction of  $\text{Co}_3\text{O}_4$  to  $\text{CoO}$  and  $\text{CoO}$  to metallic  $\text{Co}$ , respectively, are found. The increase in the  $\text{Co}$  content causes a progressive raising of intensities of these peaks and a shift in their positions to lower temperatures (finally to about 335–339 °C and 410–415 °C for MT-PAA pH 7.0 and MT-PAA pH 8.0). Similar temperatures of reduction of  $\text{Co}_3\text{O}_4$  (20 wt%) deposited on the  $\text{Al}_2\text{O}_3$ -pillared montmorillonite at 341 °C and 442 °C were earlier reported by Su et al. [60]. Obviously, the  $\text{Co}_3\text{O}_4$  nanocomposites become easily reducible when are formed in the precursors with the higher  $\text{Co}$  content. On the other hand, the opposite tendency is witnessed for the MT-PAA pH 9.0 catalyst based on the precursor obtained by  $\text{Co}(\text{OH})_2$  precipitation. The harder reduction of  $\text{Co}^{3+}$  to  $\text{Co}^{2+}$  is immediately followed by the subsequent step of deep reduction to  $\text{Co}^0$ . Consequently, only single DTG peak centered at 390 °C is observed, as was previously found by Pérez et al. [61] for  $\text{Co}_3\text{O}_4$  dispersed on the surface of delaminated  $\text{Al}_2\text{O}_3$ -modified smectite. Furthermore, all studied samples (excluding MT-PAA pH 9.0) exhibit the presence of  $\text{Co}$  species which demands temperatures above 700 °C to be reduced. Such high stability of these  $\text{Co}$  species can be explained either by the formation of cobalt aluminate/silicate [62] or the migration of  $\text{Co}^{2+}$  to the MT interlayer during the modification step forming difficulty reducible  $\text{Co}$  oxide [63]. The calculated  $\text{H}_2\text{,consum.}/\text{H}_2\text{,theor.}$  ratios (Table 2) confirm that the highest  $\text{Co}^{2+}/\text{Co}^{3+}$  stabilization effect is observed for the materials with the lowest cobalt content (MT-PAA pH 3.3 and MT-PAA pH 4.0). For other samples even less than 10% of  $\text{Co}$  species is reduced only in the high-temperature range. This reduction step is manifested by the DTG peak, which shifts from 810 °C (MT-PAA pH 3.3) to 698 °C (MT-PAA pH 8.0). For the MT-PAA pH 9.0 catalyst no distinct peak attributed to this transformation is detected.

The surface composition was additionally investigated by XPS. In Fig. 7 the  $\text{Co} 2\text{p}$  and  $\text{O} 1\text{s}$  spectra for some  $\text{Co}$ -containing materials are shown. The characteristic  $\text{Co} 2\text{p}$  doublet ( $\text{Co} 2\text{p}_{3/2}$  and  $\text{Co} 2\text{p}_{1/2}$ ) related to the spin-orbit splitting of 15.2–15.7 eV is observed. Furthermore, the deconvolution of the spectra reveals the presence of tetrahedral  $\text{Co}^{2+}$  and octahedral  $\text{Co}^{3+}$  species centered at  $781.3 \pm 0.3$  eV and  $779.9 \pm 0.3$  eV, respectively (for the  $\text{Co} 2\text{p}_{3/2}$  peak) [64]. An additional component related to multiplet splitting of  $\text{Co}^{2+}$  at  $782.4 \pm 0.3$  eV was included in the deconvolution [65]. The determined differences in the  $\text{Co}^{2+}/\text{Co}^{3+}$  molar ratio varying in the range from 1.6 to 2.5 are in reasonable agreement with the previously reported data for the surface  $\text{Co}_3\text{O}_4$  [66]. Table 1 shows the differences between  $\text{Co}/\text{Si}$  mass ratios determined in bulk and on surface of the studied samples. For the samples based on MT-PAA modified at lower pH (3.3. and 4.0) the excess amount of cobalt is detected on the external surface. The increase in pH used during the deposition causes more effective infiltration of  $\text{Co}^{2+}$  into the composite structure and consequently higher  $\text{Co}/\text{Si}$  ratios are observed in the pores of the corresponding  $\text{Co}_3\text{O}_4$ -containing catalysts. However, the sample obtained by the modification at pH = 9.0, synthesized rather by coprecipitation of  $\text{Co}(\text{OH})_2$  than selective deposition, exhibits the equal distribution of  $\text{Co}$  species on the whole surface.

The  $\text{O} 1\text{s}$  peak suggests the presence of two main  $\text{O}$ -containing species:  $\text{O}^{2-}$  lattice (binding energy of  $530.4 \pm 0.3$  eV) and hydroxyls (binding energy of  $532.4 \pm 0.2$  eV). It is found that with the increasing  $\text{Co}$  content the distribution of oxygen forms change, and more lattice ions appear in the samples (with exception of MT-PAA pH 9.0, which shows a dominant contribution of hydroxyl species).

### 3.3. Activity of calcined $\text{Co}_3\text{O}_4$ -containing catalysts in toluene combustion

The catalytic activity of the prepared  $\text{Co}_3\text{O}_4$ -containing MT materials was tested in the toluene combustion. All of them

appeared to be active and selective catalysts in the studied reaction.  $\text{CO}_2$  and  $\text{H}_2\text{O}$  were found in dominant amounts among the products, and only traces of benzene (<0.1% of selectivity) were detected for all catalysts excluding calcined MT-PAA (up to 2.4% of selectivity to benzene) and calcined MT-PAA pH 3.3 with the lowest  $\text{Co}$  content (up to 0.4% of selectivity to benzene). The observed conversions of aromatic substrate vs. the reaction temperature are shown in Fig. 8. Moreover, the values of  $T_{20}$ ,  $T_{50}$  and  $T_{90}$ , which are temperatures where 20%, 50% and 90% of toluene is converted, respectively, are presented in Table 2. It is evident that the studied materials exhibit the growing activity with the increasing  $\text{Co}_3\text{O}_4$  loading being the active phase in the studied reaction. In the case of MT, even 20% conversion of toluene is not achieved at the highest reaction temperature. For MT-PAA pH 3.3 and MT-PAA pH 4.0,  $T_{50}$  has the value of 365 °C and 313 °C, respectively, and shifts to the range of 284–288 °C for the calcined samples modified with  $\text{Co}^{2+}$  cations at pH from 5.0 to 8.0. Since the toluene combustion proceeds probably according to the Mars-van Krevelen mechanism demanding enhanced electronic transference and oxygen mobility, the catalytic activity is strongly correlated to the dispersion of  $\text{Co}_3\text{O}_4$  and its reducibility. Very promising catalytic performance is therefore obtained for the  $\text{Co}_3\text{O}_4$ -pillared clay, as was also found previously for smectite- [61] and laponite-based catalysts [67] in the total oxidation of ethanol and benzene, respectively. On the other hand, it is not surprising that  $T_{50}$  increases to 342 °C for the MT-PAA pH 9.0 catalyst exhibiting the presence of large, hardly reducible spinel crystallites. It should be also kept in mind that this sample contains a relatively high amount of Na introduced together with  $\text{Co}$  during the deposition step. Its presence can additionally suppress the catalytic activity by the unsuitable modification of  $\text{Co}_3\text{O}_4$  and/or blocking of the active sites.

The correlation between the catalytic activity of all  $\text{Co}$ -containing materials and the temperature detected in the TPR measurements as the beginning of  $\text{Co}_3\text{O}_4$  reduction is visualized in Fig. 9. It is clear that four catalysts (MT-PAA pH 5.0, MT-PAA pH 6.0, MT-PAA pH 7.0 and MT-PAA pH 8.0) with similar temperatures of  $\text{Co}_3\text{O}_4$  reduction onset (214–225 °C) and surface  $\text{Co}/\text{Si}$  mass ratio (0.56–0.72) show a comparable activity in the studied reaction. This finding strongly suggests that lattice oxygen takes part in the toluene oxidation, which proceeds over the studied  $\text{Co}$ -pillared montmorillonite catalysts according to the Mars-van Krevelen mechanism. On the other hand, it should be kept in mind that such reducibility of these samples is possible due to the appropriate dispersion of active phase. The high catalytic activity is also provided by the open pore structure formed by  $\text{Co}_3\text{O}_4$  nanoparticles pillaring the MT sheets.

Furthermore, the stability tests performed at 300 °C for 24 h for the most active catalysts (MT-PAA pH 5.0–8.0) revealed no significant changes in the observed toluene conversion. As has been previously suggested, the lack of sintering effect is a result of the separation of spinel nanoparticles by the clay platelets.

## 4. Conclusions

The hydrogel-assisted route was shown as an efficient way for the modification of clay structure by its pillaring with highly dispersed  $\text{Co}_3\text{O}_4$  nanocrystallites. In the first step, montmorillonite-poly(acrylic acid) composite was formed by the intercalation polymerization. It was shown that a part of produced polymer was introduced into the interlayer gallery. The high adsorption capacity of the synthesized composite was applied to its subsequent modification with  $\text{Co}^{2+}$  cations, which was performed at various pH within the range between 3.3 and 9.0. The higher values of pH favored the introduction of higher amounts of transition metal cations proving the interaction of  $\text{Co}^{2+}$  with dissociated car-

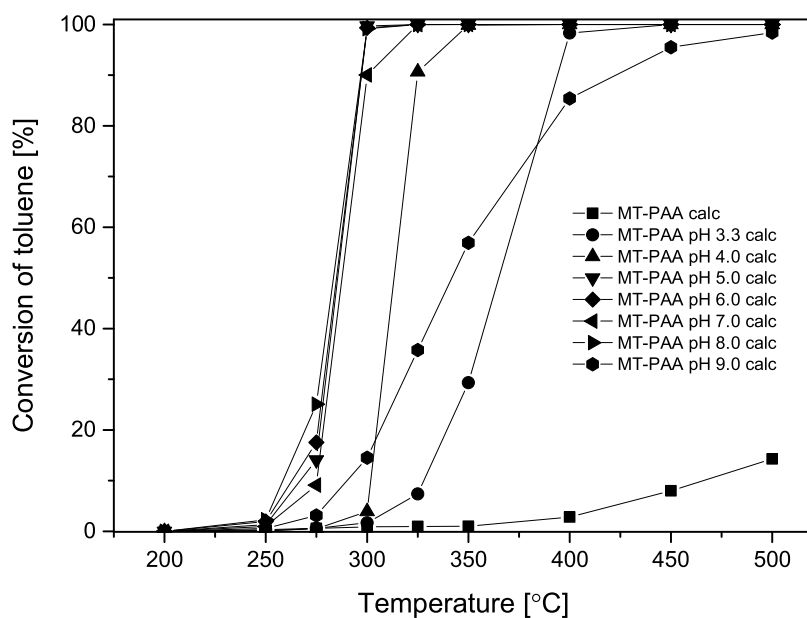


Fig. 8. Conversion of toluene over the studied materials at varying reaction temperatures.

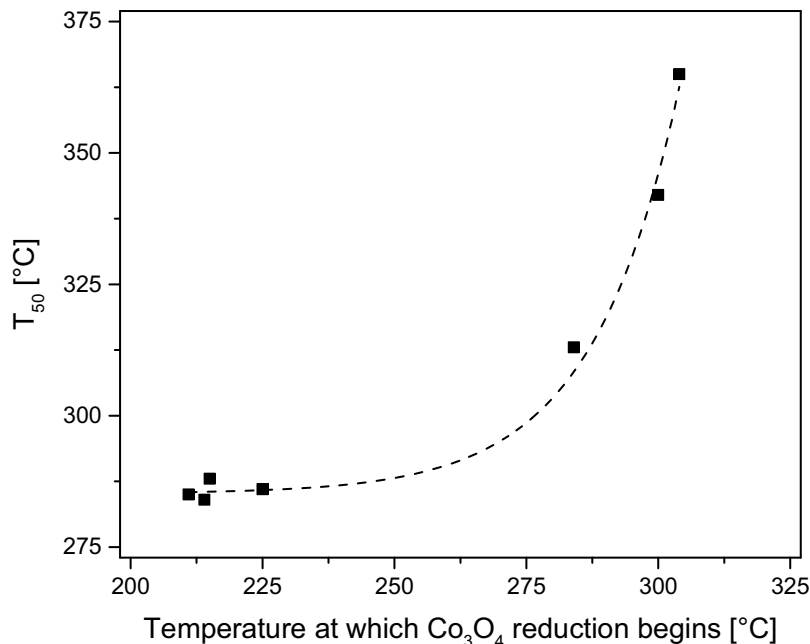


Fig. 9. Correlation between catalytic activity ( $T_{50}$ ) and temperature at which reduction of  $\text{Co}_3\text{O}_4$  begins.

boxyl groups distributed along the PAA chains. During calcination at 500 °C, the obtained Co-loaded precursors were transformed into thermally stable oxide materials, which exhibited the open pore structure formed by clay platelets pillared by nanometric  $\text{Co}_3\text{O}_4$  crystallites. This phase became easily reducible with the increase in pH used during the composite modification up to 8.0. The higher pH resulted in the formation of precipitated Co hydroxide, which after the thermal treatment formed the  $\text{Co}_3\text{O}_4$  phase characterized by the harder reducibility. The Co loading, redox properties and textural parameters appeared to be crucial factors influencing the catalytic activity of the obtained materials in the toluene combustion. This study could be considered as the first step in the development of inexpensive, active, selective and stable catalysts based on  $\text{Co}_3\text{O}_4$ -pillared clays for the VOCs combustion.

#### Acknowledgment

The research was carried out with the equipment purchased thanks to the financial support of the European Regional Development Fund in the framework of the Polish Innovation Economy Operational Program (contract No. POIG.02.01.00-12-023/08).

#### Appendix A. Supplementary data

Supplementary data associated with this article can be found, in the online version, at <http://dx.doi.org/10.1016/j.apcatb.2016.05.008>.

## References

[1] M. Amann, M. Lutz, *J. Hazard. Mater.* 78 (2000) 41–62.

[2] H. Guo, S.C. Lee, L.Y. Chan, W.M. Li, *Environ. Res.* 94 (2004) 57–66.

[3] A.P. Jones, *Atmos. Environ.* 33 (1999) 4535–4564.

[4] A. Berenjian, N. Chan, H.J. Malmiri, *Am. J. Biochem. Biotechnol.* 8 (2012) 220–229.

[5] F.I. Khan, A. Kr Ghoshal, *J. Loss Prev. Process Ind.* 13 (2000) 527–545.

[6] L.F. Liotta, *Appl. Catal. B* 100 (2010) 403–412.

[7] S. Scire, L.F. Liotta, *Appl. Catal. B* 125 (2012) 222–246.

[8] W.B. Li, J.X. Wang, H. Gong, *Catal. Today* 148 (2009) 81–87.

[9] F.N. Aguero, B.P. Barbero, L.C. Almeida, M. Montes, L.E. Cadus, *Chem. Eng. J.* 166 (2011) 218–223.

[10] R. Fiorenza, C. Crisafulli, G.G. Condorelli, F. Lupo, S. Scirè, *Catal. Lett.* 145 (2015) 1691–1702.

[11] H. Wu, L. Wang, Z. Shen, J. Zhao, *J. Mol. Catal. A* 351 (2011) 188–195.

[12] M. Hosseini, T. Barakat, R. Cousin, A. Aboukaïs, B.-L. Su, G. De Weireld, S. Siffert, *Appl. Catal. B* 111–112 (2012) 218–224.

[13] V.P. Santos, S.A.C. Carabineiro, P.B. Tavares, M.F.R. Pereira, J.J.M. Órfão, J.L. Figueiredo, *Appl. Catal. B* 99 (2010) 198–205.

[14] M. Ousmane, L.F. Liotta, G. Di Carlo, G. Pantaleo, A.M. Venezia, G. Deganello, L. Retailleau, A. Boreave, A. Giroir-Fendler, *Appl. Catal. B* 101 (2011) 629–637.

[15] A.G.M. Da Silva, H.V. Fajardo, R. Balzer, L.F.D. Probst, A.S.P. Lovón, J.J. Lovón-Quintana, G.P. Valençã, W.H. Schreine, P.A. Robles-Dutenhewer, *J. Power Source* 285 (2015) 460–468.

[16] J.C. Rooke, T. Barakat, M.F. Finol, P. Billemont, G. De Weireld, Y. Li, R. Cousin, J.-M. Giraudon, S. Siffert, J.-F. Lamonier, B.-L. Su, *Appl. Catal. B* 142–143 (2013) 149–160.

[17] F. Rahmani, M. Haghghi, P. Estifaei, *Microporous Mesoporous Mater.* 185 (2014) 213–223.

[18] P. Li, C. He, J. Cheng, C.Y. Ma, B.J. Dou, Z.P. Hao, *Appl. Catal. B* 101 (2011) 570–579.

[19] C. He, J. Li, X. Zhang, L. Yin, J. Chen, S. Gao, *Chem. Eng. J.* 180 (2012) 46–56.

[20] F.N. Aguero, B.P. Barbero, L. Gambaro, L.E. Cadus, *Appl. Catal. B* 91 (2009) 108–112.

[21] E. Genty, R. Cousin, S. Capelle, C. Gennequin, S. Siffert, *Eur. J. Inorg. Chem.* 16 (2012) 2802–2811.

[22] S.M. Saqer, D.I. Kondarides, X.E. Verykios, *Appl. Catal. B* 103 (2011) 275–286.

[23] M.H. Castaño, R. Molina, S. Moreno, *J. Mol. Catal. A* 398 (2015) 358–367.

[24] D.A. Aguilera, A. Perez, R. Molina, S. Moreno, *Appl. Catal. B* 104 (2011) 144–150.

[25] F. Wang, H. Dai, J. Deng, G. Bai, K. Ji, Y. Liu, *Environ. Sci. Technol.* 46 (2012) 4034–4041.

[26] K. Jirátová, J. Mikulová, J. Klempa, T. Grygar, Z. Bastl, F. Kovanda, *Appl. Catal. A* 361 (2009) 106–116.

[27] H.-F. Lu, Y. Zhou, W.-F. Han, H.-F. Huang, Y.-F. Chen, *Appl. Catal. A* 464–465 (2013) 101–108.

[28] X. Fan, T.L. Zhu, M.Y. Wang, X.M. Li, *Chemosphere* 75 (2009) 1301–1306.

[29] S. Behar, N.-A. Gómez-Mendoza, M.-A. Gómez-García, D. Świerczyński, F. Quignard, N. Tanchoux, *Appl. Catal. A* 504 (2015) 203–210.

[30] A. Giroir-Fendler, M. Alves-Fortunato, M. Richard, C. Wang, J.A. Diaz, S. Gil, C. Zhang, F. Can, N. Bion, Y. Guo, *Appl. Catal. B* 180 (2016) 29–37.

[31] A. Białas, P. Kuśtrowski, B. Dudek, Z. Piwowarska, A. Wach, M. Michalik, M. Kozak, *Thermochim. Acta* 590 (2014) 191–197.

[32] A. Białas, P. Niebrzydowska, B. Dudek, Z. Piwowarska, L. Chmielarz, M. Michalik, M. Kozak, P. Kuśtrowski, *Catal. Today* 176 (2011) 413–416.

[33] A.M. Carrillo, J.G. Carriazo, *Appl. Catal. B* 164 (2015) 443–452.

[34] U. Menon, V.V. Galvita, G.B. Marin, *J. Catal.* 283 (2011) 1–9.

[35] Á. Szegedi, M. Popova, K. Lázár, S. Klébert, E. Drotár, *Microporous Mesoporous Mater.* 177 (2013) 97–104.

[36] R. Pereñiguez, J.L. Hueso, F. Gaillard, J.P. Holgado, A. Caballero, *Catal. Lett.* 142 (2012) 408–416.

[37] M. Popova, A. Szegedi, Z. Cherkezova-Zheleva, A. Dimitrova, I. Mitov, *Appl. Catal. A* 381 (2010) 26–35.

[38] K. Ji, H. Dai, J. Deng, H. Zhang, L. Zhang, H. Jiang, *Solid State Sci.* 27 (2014) 36–42.

[39] M. Popova, A. Szegedi, Z. Cherkezova-Zheleva, I. Mitov, N. Kostova, T. Tsonecheva, *J. Hazard. Mater.* 168 (2009) 226–232.

[40] B. Xue, H. Guo, L. Liu, M. Chen, *Clay Miner.* 50 (2015) 211–219.

[41] T. Barakat, J.C. Rooke, H.L. Tidahy, M. Hosseini, R. Cousin, J.-F. Lamonier, J.-M. Giraudon, G. De Weireld, B.-L. Su, S. Siffert, *ChemSusChem* 4 (2011) 1420–1430.

[42] B. Silva, H. Figueiredo, V.P. Santos, M.F.R. Pereira, J.L. Figueiredo, A.E. Lewandowska, M.A. Bañares, I.C. Neves, T. Tavares, *J. Hazard. Mater.* 192 (2011) 545–553.

[43] X. Wang, X. Chen, L. Gao, H. Zheng, Z. Zhang, Y. Qian, *J. Phys. Chem. B* 108 (2004) 16401–16404.

[44] Q. Liu, L.C. Wang, M. Chen, Y. Cao, H.Y. He, K.N. Fan, *J. Catal.* 263 (2009) 104–113.

[45] B. Solsona, T.E. Davies, T. García, I. Vázquez, A. Dejoz, S.H. Taylor, *Appl. Catal. B* 84 (2008) 176–184.

[46] T. García, S. Agouram, J.F. Sánchez-Royo, R. Murillo, A.M. Mastral, A. Aranda, I. Vázquez, A. Dejoz, B. Solsona, *Appl. Catal. A* 386 (2010) 16–27.

[47] D.M. Gómez, V.V. Galvita, J.M. Gatica, H. Vidal, G.B. Marin, *Phys. Chem. Chem. Phys.* 16 (2014) 11447–11455.

[48] S. Zuo, Q. Huang, R. Zhou, in: A. Gil, S.A. Korili, R. Trujillano, M.A. Vicente (Eds.), *Pillared Clays and Related Catalysts*, Springer-Verlag, New York, 2010, pp. 225–254.

[49] P. Natkański, P. Kuśtrowski, A. Białas, A. Wach, A. Rokicińska, M. Kozak, L. Lityńska-Dobrzańska, *Microporous Mesoporous Mater.* 221 (2016) 212–219.

[50] N.H. Tran, G.R. Dennis, A.S. Milev, G.S. Kamali Kannangara, M.A. Wilson, R.N. Lamb, *J. Colloid Interface Sci.* 290 (2005) 392–396.

[51] N.H. Tran, M.A. Wilson, A.S. Milev, G.R. Dennis, G.S.K. Kannangara, R.N. Lamb, *Sci. Technol. Adv. Mater.* 7 (2006) 786–791.

[52] P. Natkański, P. Kuśtrowski, A. Białas, Z. Piwowarska, M. Michalik, *Mater. Chem. Phys.* 136 (2012) 1109–1115.

[53] P. Natkański, P. Kuśtrowski, A. Białas, Z. Piwowarska, M. Michalik, *Appl. Clay Sci.* 75–76 (2013) 153–157.

[54] J. Madejová, *Vib. Spectrosc.* 31 (2003) 1–10.

[55] J. Dong, Y. Ozaki, K. Nakashima, *Macromolecules* 30 (1997) 1111–1117.

[56] A.A. Zaman, R. Suchiya, B.M. Moudgil, *J. Colloid Interface Sci.* 256 (2002) 73–78.

[57] I. Sabbagh, M. Delsanti, *Eur. Phys. J. E* 1 (2000) 75–86.

[58] J.R.S. Brownson, C. Lévy-Clément, *Electrochim. Acta* 54 (2009) 6637–6644.

[59] L.G.A. van de Water, G.L. Bezemer, J.A. Bergwerff, M. Versluijs-Helder, B.M. Weckhuysen, K.P. de Jong, *J. Catal.* 242 (2006) 287–298.

[60] H. Su, S. Zeng, H. Dong, Y. Du, Y. Zhang, R. Hu, *Appl. Clay Sci.* 46 (2009) 325–329.

[61] A. Pérez, M. Montes, R. Molina, S. Moreno, *Appl. Clay Sci.* 95 (2014) 18–24.

[62] Y.-H. Zhao, Y.-H. Song, Q.-Q. Hao, Y.-J. Wang, W. Wang, Z.-T. Liu, D. Zhang, Z.-W. Liu, Q.-J. Zhang, J. Lu, *Fuel Process. Technol.* 138 (2015) 116–124.

[63] Q.-Q. Hao, G.-W. Wang, Y.-H. Zhao, Z.-T. Liu, Z.-W. Liu, *Fuel* 109 (2013) 33–42.

[64] M.C. Biesinger, B.P. Payne, A.P. Grosvenor, L.W.M. Lau, A.R. Gerson, R.S.C. Smart, *Appl. Surf. Sci.* 257 (2011) 2717–2730.

[65] V. Iablokov, R. Barbosa, G. Pollefeyt, I. Van Driessche, S. Chenakin, N. Kruse, *ACS Catal.* 5 (2015) 5714–5718.

[66] Ž. Chromáková, L. Obalová, F. Kovanda, D. Legut, A. Titov, M. Ritz, D. Fridrichová, S. Michalik, P. Kuśtrowski, K. Jirátová, *Catal. Today* 257 (2015) 18–25.

[67] J.J. Li, Z. Mu, X.Y. Xu, H. Tian, M.H. Duan, L.D. Li, Z.P. Hao, S.Z. Qiao, G.Q. Lu, *Microporous Mesoporous Mater.* 114 (2008) 214–221.